


# Electrical investigation and enhancement of optical, structural, and dielectric properties of flexible PVDF/LiZnVO<sub>4</sub> nanocomposites

I. S. Elashmawi<sup>1</sup> · A. M. Ismail<sup>1</sup> · A. M. Abdelghany<sup>1</sup> · M. M. Hegazi<sup>2</sup> · A. Y. Yassin<sup>3</sup>

Received: 28 February 2023 / Accepted: 15 June 2023

Published online: 31 July 2023

© The Author(s) 2023 

## Abstract

Thin polymeric films of poly(vinylidene fluoride) (PVDF) containing variable mass fractions of nanoparticles (LiZnVO<sub>4</sub>) were successfully synthesized via the ordinary solution casting method. X-ray diffraction (XRD), Fourier transform infrared (FT-IR), and ultraviolet–visible spectroscopy were used to explore the role of LiZnVO<sub>4</sub> on the structural and optical characteristics of synthesized nanocomposites. In addition, dielectric permittivity ( $\epsilon'$  and  $\epsilon''$ ) and dielectric modulus ( $M'$  and  $M''$ ) were investigated. The XRD spectral data reveals the crystalline nature of pure LiZnVO<sub>4</sub> with rhombohedral structure with an average size of 83 nm calculated using the Scherrer's equation and W-L plot. The interaction between PVDF and LiZnVO<sub>4</sub> was approved through the shift in characteristics in some IR bands. The decrease in band gap energies with increasing LiZnVO<sub>4</sub> was attributed to the change of density in the localized states within the PVDF matrix. The effect of both frequency and temperature on the AC parameters was also investigated. Both  $\epsilon'$  and  $\epsilon''$  had their maximum values at low frequencies and decreased as the frequency and temperature increased. The results from XRD and FT-IR were correlated with changes in the dielectric characteristics at the maximum level value of LiZnVO<sub>4</sub>, suggesting the potential of these materials as basic components for lithium-ion batteries.

**Keywords** LiZnVO<sub>4</sub> nanoparticles · X-ray diffraction · FT-IR · UV–Visible · AC electrical modulus

## 1 Introduction

Modern technologies are concerned with the use of lithium-ion polymer batteries as an alternative to the liquid electrolytic battery, which is used as an electrolyte and as a separator [1–4]. This is because the polymeric structure batteries used in the production of batteries greatly help in enhancing safety and security. This is because of the problems that liquid electrolytes come from, such as the decomposition of the liquid and the rise of gases. Generally, polymer film composites are used in lithium batteries for their thermal and electrochemical stability, and good mechanical strength [5–7].

Poly(vinylidene fluoride) (PVDF) is a commonly used polymer in lithium battery applications [8–10]. PVDF contains a large concentration of charge carriers as a result of the strong electron-withdrawing properties of its functional group (–C–F) and its high anodic stability [11]. PVDF is receiving great attention for its piezoelectric properties when compared to any other polymer [12]. PVDF is widely used in energy-related applications and specialties. Pure PVDF has many properties such as high chemical resistance, outstanding mechanical strength, piezoelectric, and thermoelectric properties.

✉ I. S. Elashmawi, islam\_shukri2000@yahoo.com | <sup>1</sup>Spectroscopy Department, Physics Research Institute, National Research Centre, ElBehouth St., Giza 12311, Dokki, Egypt. <sup>2</sup>Department of Basic Science, Mansoura Higher Institute of Engineering and Technology, Mansoura, Egypt. <sup>3</sup>Department of Basic Sciences, Delta University for Science and Technology, Gamassa, Mansoura, Egypt.



PVDF is used in many electronic applications and as sheathing for cables used in audio, video, and alarm systems. Lithium-ion polymer systems employ PVDF as a battery separator and as a binder for the anodes and cathodes [13–18].

Research on materials used as anode confirms that  $\text{LiZnVO}_4$  with specific nanoscale sizes can be used in the lithium-ion secondary battery as the negative electrode [19]. Several studies of the synthesis and characterization of PVDF/ $\text{LiZnVO}_4$  materials. The authors investigate their structural, optical, and electrical properties and they showed that the addition of  $\text{LiZnVO}_4$  nanoparticles led to improved crystallinity, optical transparency, and electrical conductivity of the PVDF nanocomposites. The authors suggest that these materials could be useful in the development of energy storage devices and optoelectronic applications. And they suggested that these materials could be used in the development of high-performance lithium-ion batteries, as well as their potential applications in various fields [19–21]. Khichar et al. were study the structural, optical, and surface morphological studies of ethyl cellulose (EC)/GO nanocomposites [22]. Dhayal et al. prepatigate of structural and electrical properties of novel and biodegradable Chitosan-GO (CS/GO) polymer nanocomposites [23].

At present, polymeric nanomaterials containing nanoparticles additive are prepared and used, which makes them develop and improve functions within the polymeric matrices [24, 25]. The Li-ion battery technology is an emerging technology for powering microelectronic devices for their large volumetric and power capacities with large progressive life and low discharge rates. Since the reduction of the volume of lithium batteries with liquid electrolytes. Solid-state batteries are an alternative with the availability of easy kinetics of diffusion of Li within the polymer [26–30]. The use of PVDF/ $\text{LiZnVO}_4$  materials has shown great potential in the development of high-performance lithium-ion batteries. The addition of  $\text{LiZnVO}_4$  nanoparticles to PVDF thin films has resulted in improved structural and optical characteristics, as well as enhanced AC conductivity and dielectric properties. These improvements are attributed to the interaction between the PVDF and  $\text{LiZnVO}_4$ , which leads to changes in the localized states within the PVDF and a decrease in band gap energies. These materials could be utilized as basic components in the fabrication of advanced energy storage devices, such as lithium-ion batteries, due to their promising performance and characteristics. This work initially aims to prepare  $\text{LiZnVO}_4$  nanoparticles, and then incorporate them in PVDF using the casting method (as a simple blending) for solid rechargeable battery applications. The effect of  $\text{LiZnVO}_4$  on the structural and optical properties within the polymeric matrix is studied using XRD, FT-IR, and UV–VIS techniques. Moreover, the electrical conductivity properties of the prepared films were studied in detail.

## 2 Materials and methods

### 2.1 Materials

Both the PVDF ( $\text{CH}_2\text{CF}_2$ ,  $M_w = 543,000$ ) and the  $\text{LiZnVO}_4$  were kindly supplied by Sigma Aldrich. Dimethyl sulfoxide (DMSO) was obtained from S. D. Fine-Chem Limited.

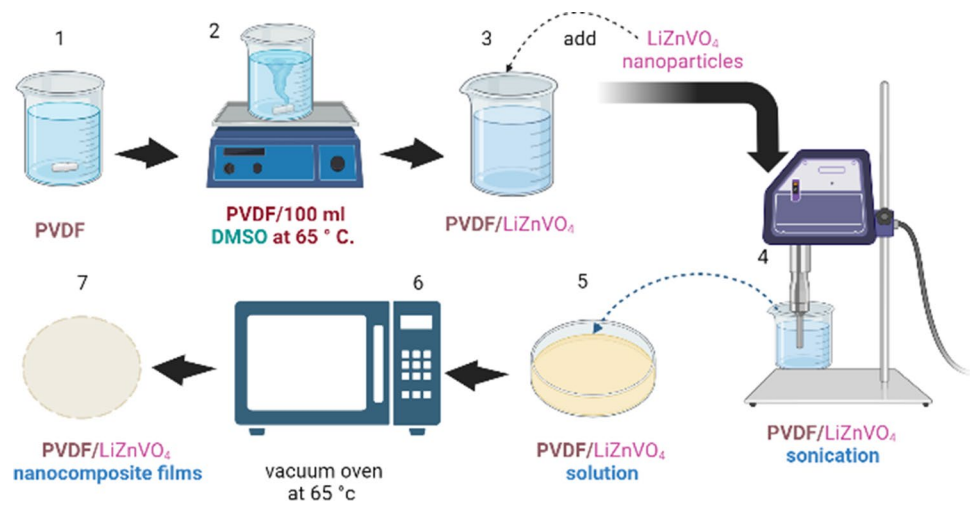
### 2.2 Preparation of PVDF/ $\text{LiZnVO}_4$ composite membranes

Two grams of PVDF were mixed into 100 ml of DMSO at 65 °C. After that, 3, 5, and 10 wt. % of  $\text{LiZnVO}_4$  nanoparticles were added step by step to the polymeric solution. Then, the suspension was first sonicated to keep the particles from sticking together in the PVDF solution. It was then stirred constantly at 65 °C until a homogeneous solution was made. To remove the solvent, the resulting solutions were poured onto Petri plates and put in a vacuum oven at 65 °C for about 12 h. The PVDF/ $\text{LiZnVO}_4$  nanocomposites were made into thin films that were about 20  $\mu\text{m}$  thick. BioRender a software is a tool for creating scientific graphics and illustrations the steps of the experimental procedure for the preparation of PVDF/GO nanocomposites as shown in Scheme 1.

### 2.3 Measurement techniques

The X-ray diffraction measurements were done with a PANalytical X'Pert Pro running at 45 kV and using a Cu-K $\alpha$  target with secondary monochromator Holland radiation at  $\lambda = 0.1540$  nm with  $2\theta = 5\text{--}70^\circ$ . We used a Bruker VERTEX 80 (Germany) combined platinum-diamond ATR, which has a diamond disc as an internal reflector in the range 4000–400  $\text{cm}^{-1}$  with a resolution of 4  $\text{cm}^{-1}$  and a total of 50 scans, to take ATR-FTIR measurements. A Jasco V-630 UV–VIS (Japan) spectrophotometer was used to look at absorption spectra in the ultraviolet–visible spectrum. To measure the AC conductivity,

**Scheme 1** Steps of the experimental procedure for the preparation of PVDF/GO nanocomposites



a Broadband dielectric spectroscopy (BDS) type (concept 40) novocontrol high-resolution alpha analyzer was used with four temperature controllers.

### 3 Results and discussion

#### 3.1 The X-ray diffraction (XRD)

The XRD patterns of pure PVDF and the PVDF/LZV-NPs nanocomposites with varying concentrations of LZV-NPs are shown in Fig. 1. The diffraction peaks appeared at about 19°, 21° and 40° which are ascribed to PVDF host polymer. [31–33]. According to JCPDS Card No. 38-1332, the XRD spectrum of LiZnVO<sub>4</sub> shows a rhombohedral structure. Scherrer's equation was used to determine the crystallite size of LiZnVO<sub>4</sub>. This equation has the form  $C = [(K\lambda)/(\beta\cos\theta)]$ , where C is the crystallite size, K is a constant equal to 0.9 and  $\lambda$  is the X-ray wavelength.  $\theta$  is the diffraction angle and  $\beta$  is the full width at half maximum of diffraction pcomputeomputing the mean crystallite size, intense diffraction peaks were chosen, and the result was determined to be 83 nm.

The interaction between PVDF and LiZnVO<sub>4</sub> NPs is confirmed by shifting the diffraction peak of PVDF at  $2\theta = 20.7^\circ$  with a variation in its broadening and intensity. The diffraction peaks of LiZnVO<sub>4</sub> begin to appear and their intensities

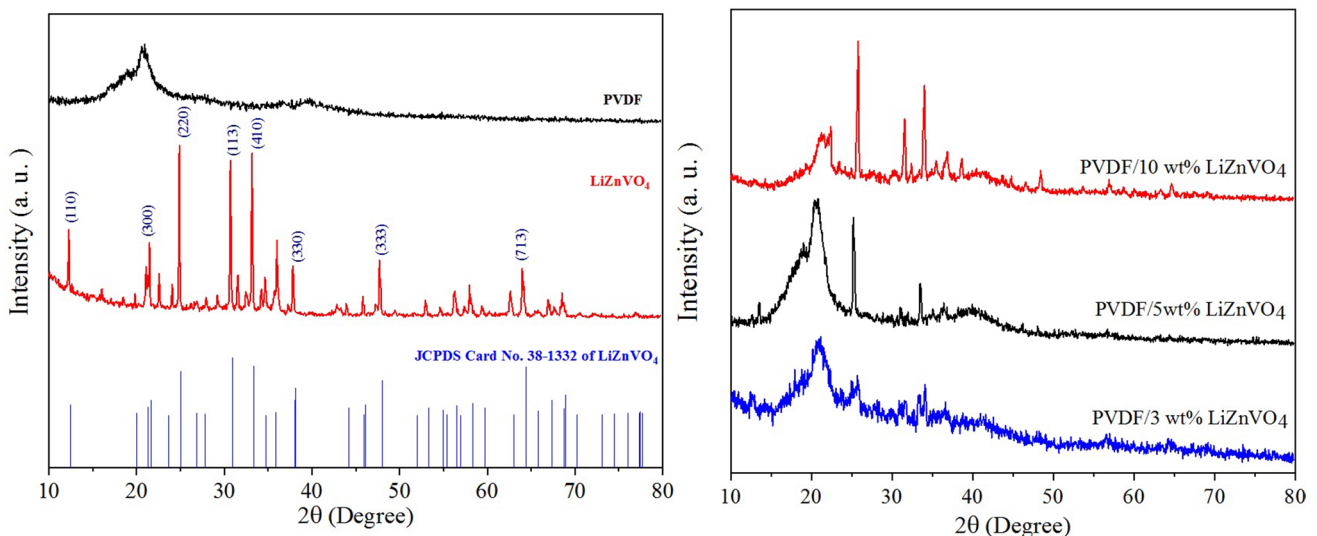


**Fig. 1** XRD of PVDF and PVDF doped with a different weight percentage of LiZnVO<sub>4</sub>

increase with increasing the weight percentage of LiZnVO<sub>4</sub> NPs with shifting in their position that is related to LiZnVO<sub>4</sub> NPs. This indicates the interaction between PVDF and LiZnVO<sub>4</sub> NPs.

The size and strain broadening by considering peak width as a function of 2θ of the samples is calculated from the Williamson-Hall (W-L) plot. W-L plots are a type of graphical analysis used to extract information about the microstructure of a crystalline material from its X-ray diffraction pattern.

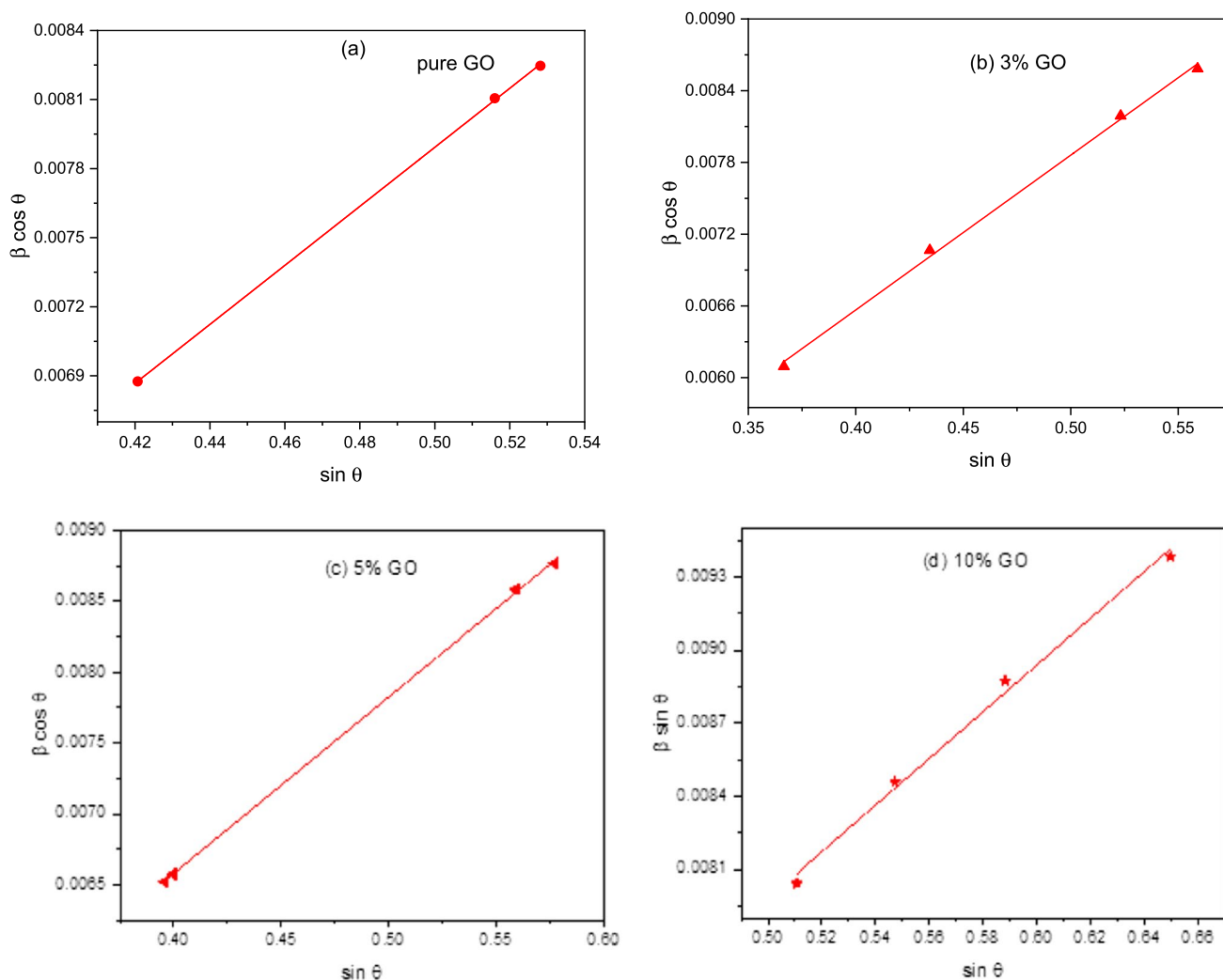
The broadening of peaks is written as [22, 23]:

$$\beta = \beta_D + \beta_\epsilon = \beta_D = \frac{k\lambda}{D\cos\theta} + \epsilon\tan\theta \tag{1}$$

where k=0.9 is a constant and λ=0.15406 nm is the wavelength of the X-ray source. A final form of the Eq. (1) is obtained as:

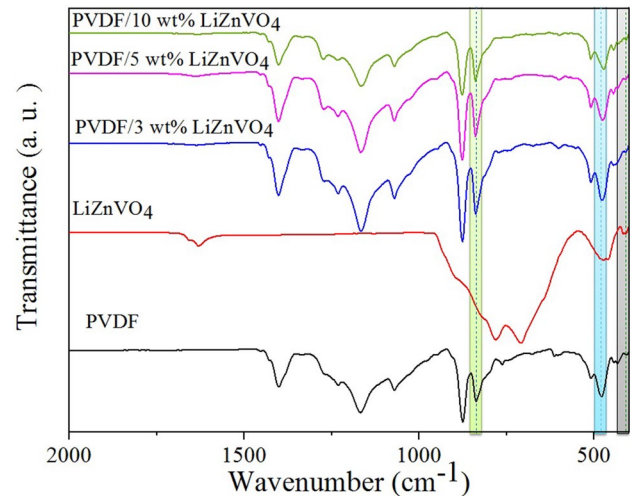
$$\beta\cos\theta = \frac{k\lambda}{D} + \epsilon\sin\theta \tag{2}$$

Figure 2a–d shows the W-L plot of pure GO and PVDF incorporated with 3, 5, and 10% wt.% of GO. The estimated data points are fitted with a distinct straight line. The slope of the linear portion of the W-L plot is related to the crystallite size, while the y-intercept ( $\frac{k\lambda}{D}$ ) is related to the strain within the crystallites. According to the figure, an inverse relationship is observed between the concentration of LiZnVO<sub>4</sub> and strain while an increase of the crystallite size. This may be

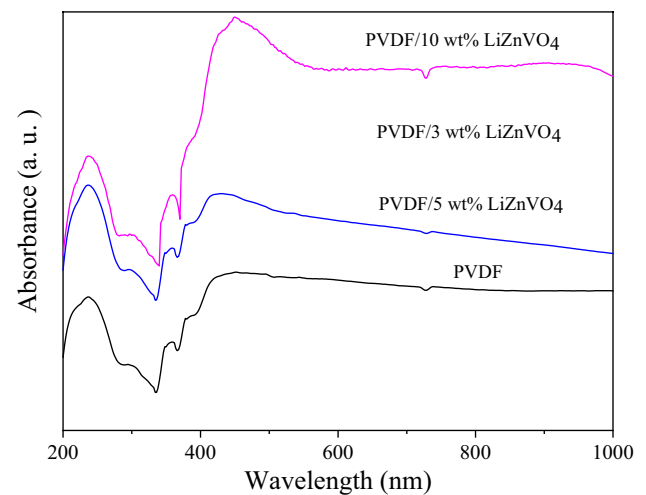


**Fig. 2 a–d** The W-L plot of pure GO and PVDF incorporated with 3, 5, and 10% wt.% of GO

**Fig. 3** FT-IR of PVDF and PVDF doped with a different weight percentage of LiZnVO<sub>4</sub>



**Fig. 4** UV-Vis spectra of PVDF and PVDF doped with a different weight percentage of LiZnVO<sub>4</sub>



attributed to the presence of crystallite nature crystallite of LiZnVO<sub>4</sub>, which could be distribution of LiZnVO<sub>4</sub> in PVDF polymeric matrices.

### 3.2 Fourier transform infrared (FT-IR)

Figure 3 represents the FT-IR of pure PVDF and PVDF incorporated with different weight percentages of LiZnVO<sub>4</sub>. PVDF exhibits bands at 1402 cm<sup>-1</sup> and 1071 cm<sup>-1</sup> which are attributable to the wagging mode of CH<sub>2</sub> [34, 35]. The CF<sub>2</sub> asymmetric stretching vibration is found at 1234 cm<sup>-1</sup> and 1168 cm<sup>-1</sup>. The C-C asymmetric vibration is observed at 875 cm<sup>-1</sup>. The CH<sub>2</sub> rocking vibration is visible at 834 cm<sup>-1</sup>. The CF<sub>2</sub> bending vibrations are shown at 613 cm<sup>-1</sup>, 510 cm<sup>-1</sup> and 477 cm<sup>-1</sup> [31–33]. LiZnVO<sub>4</sub> has bands at 780 cm<sup>-1</sup> and 710 cm<sup>-1</sup> which are related to V-O stretching vibration. The band at 414 cm<sup>-1</sup> is related to the stretching vibration of Zn-O. The stretching vibration of Li-VO<sub>4</sub> is observed at 476 cm<sup>-1</sup>. The interaction between PVDF and LiZnVO<sub>4</sub> is approved by shifting the band from 834 cm<sup>-1</sup> to 840 cm<sup>-1</sup> and shifting the band from 477 cm<sup>-1</sup> to 471 cm<sup>-1</sup> with a new band at 409 cm<sup>-1</sup>.

### 3.3 Ultraviolet-Visible measurement

Figure 4 shows UV-Visible spectra of pure PVDF and PVDF incorporated with a different weight percentage of LiZnVO<sub>4</sub> in the wavelength range of 190–800 nm. The optical absorption edge can be described using these spectra. All spectra

have an intense absorption band at 237 nm. The intensity of this band has increased and the broadening decreased with increasing the weight percentage of  $\text{LiZnVO}_4$  which indicated that there is an interaction between PVDF and  $\text{LiZnVO}_4$ .

Direct and indirect band gaps are the parameters that categorize polymers with doped fillers. The highest point of the valence band and the lowest point of the conduction band both lie at zero crystal momentum in the case of a direct band gap. Indirect conduction is referred to as conduction in which the bottom of the conduction band does not relate to zero crystal momentum. While in materials with an indirect band gap, the transition from the valence band to the conduction band should be coupled with phonons with the appropriate crystal momentum magnitude. Near the fundamental band edge, the relations between  $(\alpha h\nu)^2$  and  $(\alpha h\nu)^{1/2}$  against photon energy  $h\nu$  [36, 37] facilitate to determine whether a transition is direct or indirect according to the following relation.

$$(\alpha h\nu) = B (h\nu - E_g)^{1/n} \quad (3)$$

where  $E_g$  is the band gap energy and B is constant.  $\alpha$  is the absorption coefficient calculated from  $2.303A/d$  where A is the absorbance and d is the thickness of the prepared films. Plotting  $\alpha$  against  $h\nu$  gives the value of absorption edge as seen in Fig. 5. n has a different value of 2 or 1/2 according to the type of transition (Hussein et al. [39]; Salem et al. 2022; Nouh and Benthami [38]).

for allowed indirect transition

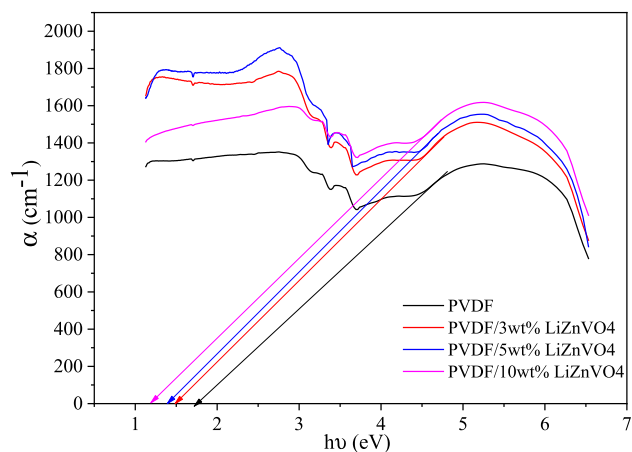
$$(\alpha h\nu) = B (h\nu - E_{gin})^2 \quad (4)$$

for allowed direct transition

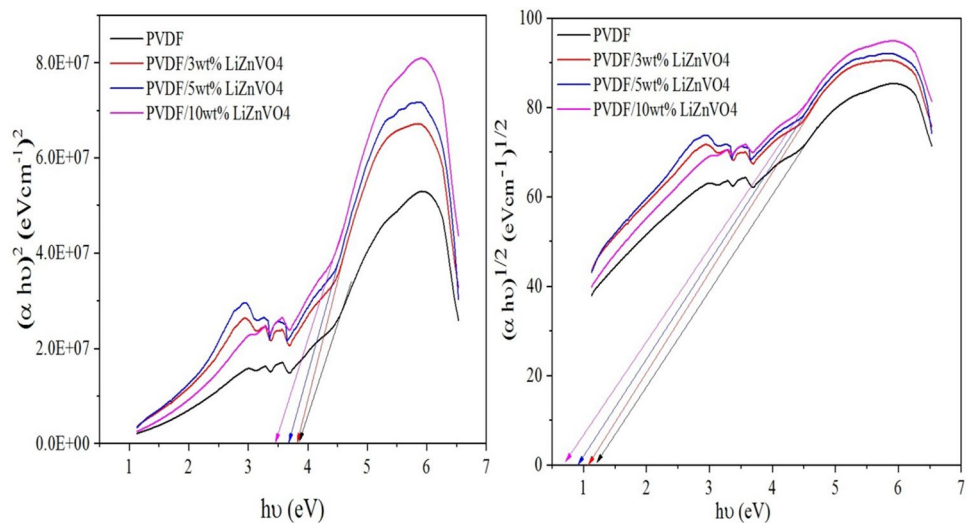
$$(\alpha h\nu) = B (h\nu - E_{gd})^{1/2} \quad (5)$$

Figure 6 represents the relation between  $(\alpha h\nu)^2$  and  $(\alpha h\nu)^{1/2}$  against photon energy  $h\nu$ . The value of the optical band gap energy can be determined by finding the intercept of the extension of the linear component of these curves to zero absorption on the axis. The obtained values are shown in Fig. 7. It is observed that band gap energies are significantly decreased with increasing  $\text{LiZnVO}_4$ . This decrease originated from the numerous polaronic contributions and imperfections within the PVDF-based nanocomposites. Some previous work has also shown how the integration of nanofillers in polymeric matrix results in a decrease in optical band gap [35, 40]. New energy levels (traps) have been created between the HOMO and LOMO, which has led to a fall in values. This is a consequence of the formation of disorder. As a result, the density of the localized states in the mobility band gap of the PVDF is increased.

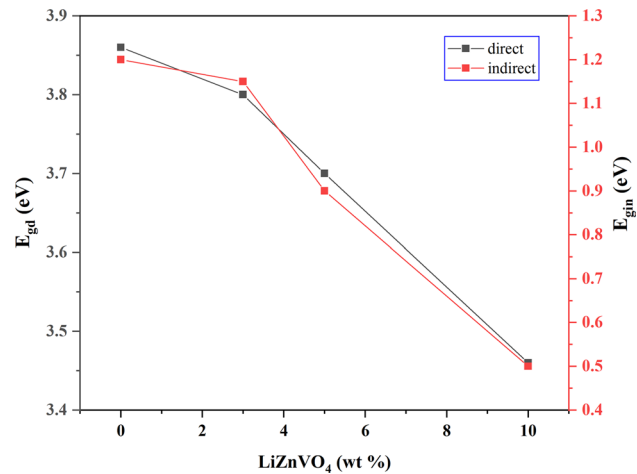
**Fig. 5** Relation between absorption coefficient against photon energy of PVDF and PVDF doped with a different weight percentage of  $\text{LiZnVO}_4$



**Fig. 6** Relation between  $(ah\nu)^2$  and  $(ah\nu)^{1/2}$  against photon energy of PVDF and PVDF doped with a different weight percentage of  $\text{LiZnVO}_4$



**Fig. 7** The dependence of optical energy gaps on different weight percentage of  $\text{LiZnVO}_4$



### 3.4 Dielectric studies

#### 3.4.1 Dielectric permittivity analysis

As a function of the frequency and temperature, the dielectric behavior of the PVDF polymer filled with different concentrations of  $\text{LiZnVO}_4$  is investigated. The frequency ranged from 0.1 Hz to 7 MHz, and the temperature varied between 30 and 120 °C. The following formula is used to represent the real ( $\epsilon'$ ) and imaginary ( $\epsilon''$ ) components of the dielectric permittivity [41–44];

$$\epsilon' = \frac{C_e d}{\epsilon_0 A} \text{ and } \epsilon'' = \frac{\sigma}{2\pi f \epsilon_0} \tag{6}$$

where  $C_e$  is the capacitance experimentally obtained for a sample under investigation,  $d$  is the sample thickness  $A$  is the used electrode's cross-sectional area, and  $\epsilon_0$  is the free space's permittivity.

Over the above ranges, Figs. 8 and 9 show the  $\epsilon'$  and  $\epsilon''$  curves as a function of frequency. At low frequencies, both parameters ( $\epsilon'$  and  $\epsilon''$ ) had their maximum values and began to decrease as the frequency increased. Since  $\epsilon'$  and  $\epsilon''$  have better values when the applied temperature is raised, it is evident that they are temperature-dependent properties.

It is worth mentioning that the high  $\epsilon'$  values achieved for frequency  $> 10^2$  Hz have been ascribed to the induced dipoles' ability to follow the periodic change in the field direction employed. This alteration is slow; thus, it provides the current dipoles sufficient time to align themselves with/against the direction of the applied field. The reaction gave rise

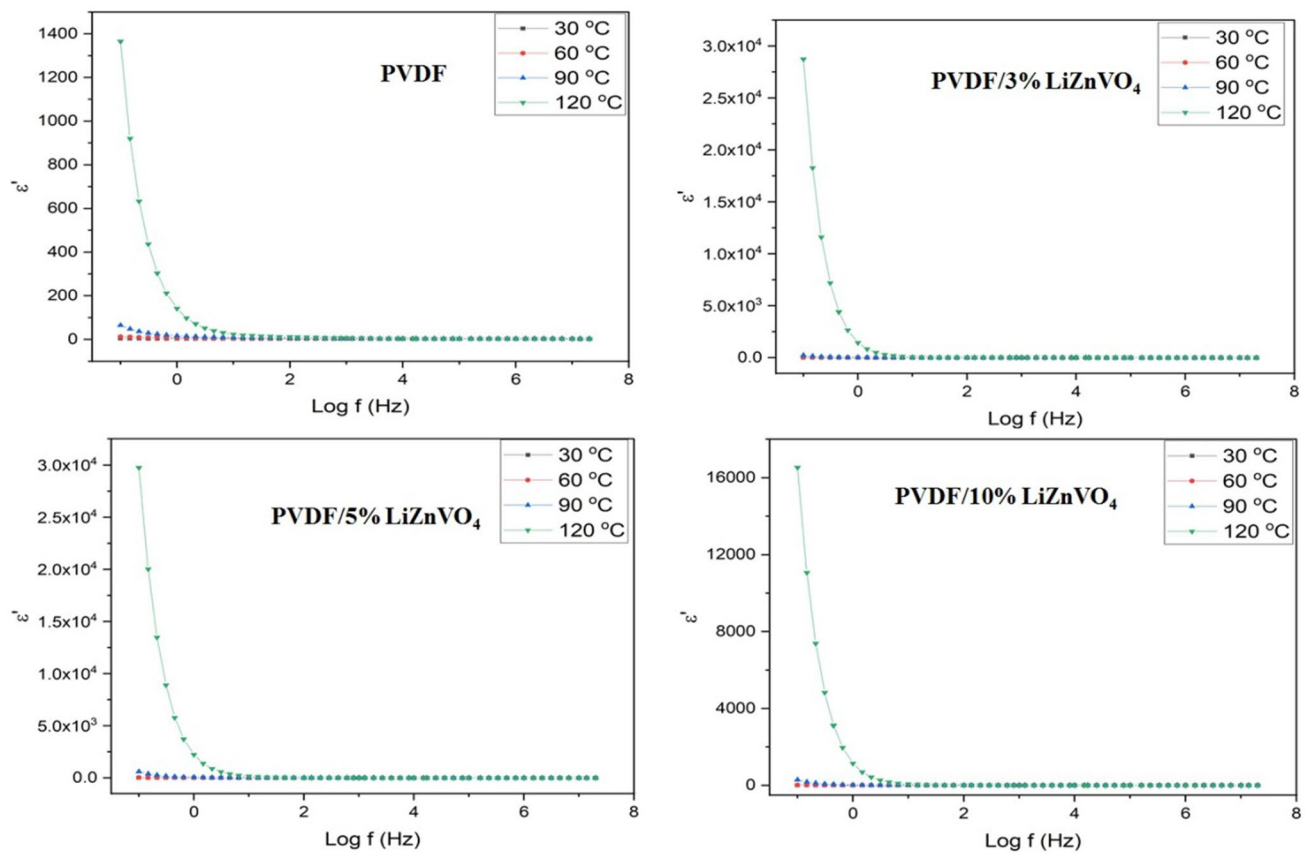


**Fig. 8** The  $\epsilon'$  curves of PVDF and PVDF doped with a different weight percentage of LiZnVO<sub>4</sub> samples as a function of temperature and frequency

to a significant increase in interfacial polarization, which brought about the current nanocomposite films having excellent dielectric characteristics.

On the contrary, the substantial drop in the  $\epsilon'$  values in the high-frequency area was attributed to charge carriers' inability to alter their direction in response to the applied field, leading to the gradual accumulation of ions in the area between PVDF and LiZnVO<sub>4</sub>, hence reducing the interfacial polarization. Thus, we can conclude that the minor fluctuations in the  $\epsilon'$  and  $\epsilon''$  with frequency, see Figs. 8 and 9, result from the minimal efficacious impact of ionic polarization combined with the lower contribution of electronic polarization. Additionally, this negligible variation is responsible for the dielectric relaxation responses occurring inside the current matrices [45–47]. So, the introduction of LiZnVO<sub>4</sub> nanofiller into the PVDF host matrix improved the samples' dielectric properties, particularly the one which contains 5 wt% of LiZnVO<sub>4</sub>, which confirms the XRD finding.

The minimum value of the dielectric loss is because of the existence of thin strata of PVDF that function as a protective covering for the Li-ions. This coverage minimizes current leakage caused by direct contact with Li-ions, while also confirming the reasonable compatibility between the LiZnVO<sub>4</sub> and the PVDF matrix. PVDF is a dielectric substance, whereas LiZnVO<sub>4</sub> is a conductive material. Therefore, doping PVDF with the nanofiller resulted in the micro-capacitors formation within the present films.

### 3.4.2 Dielectric relaxation behavior

Figure 10 shows the frequency dependence of the loss tangent ( $\tan \delta$ ) of PVDF/ LiZnVO<sub>4</sub> films at 30 °C. To further understand the dielectric relaxation responses happening within the PVDF-based films, it is necessary to investigate this dependence in detail. Loss tangent value is the ratio of  $\epsilon''$  to  $\epsilon'$  for the nanocomposite film under study. The relaxation peaks that distinguish this figure, especially for the samples containing Li-ions at high temperatures, are attributed to the relaxation response of dipoles inside the polymer parts as a consequence of the complexation



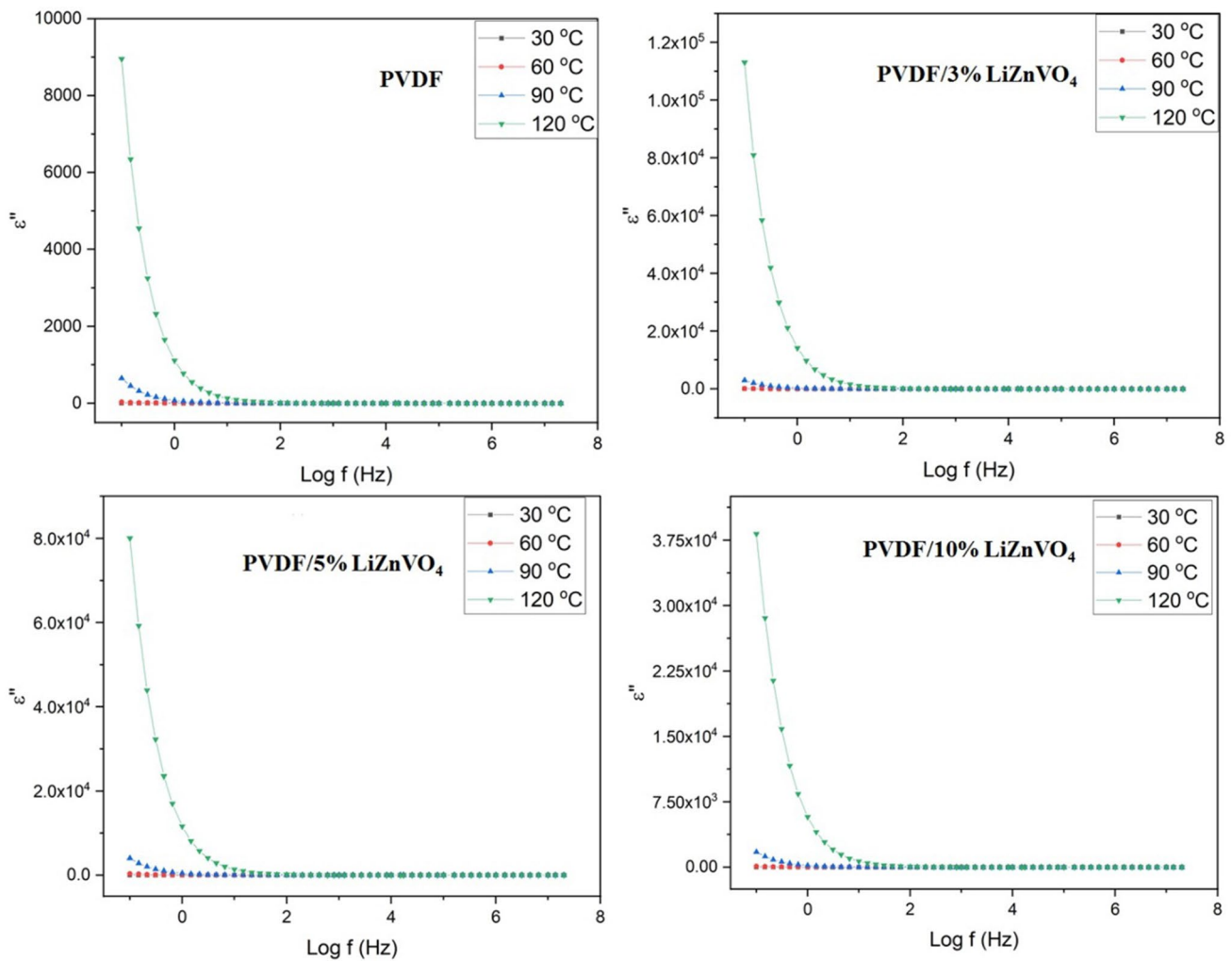


**Fig. 9** The  $\epsilon''$  curves of PVDF and PVDF doped with a different weight percentage of LiZnVO<sub>4</sub> samples as a function of temperature and frequency

between induced ions and dipoles. The appearance of this peak verifies the semicrystalline structure of the PVDF and suggests that ionic conduction dominates within doped with LiZnVO<sub>4</sub>. As a consequence of the  $\alpha$ -relaxation process, which is accompanied by the rotational movement of functional groups scattered around the central chain axis, this mode has been localized in the low-frequency area. Further, the observed change in the peak position toward higher frequencies with increasing temperature is attributable to the dominance of amorphous areas within the PVDF host matrices. In other words, the obvious movement of the peak into the high-frequency area implies that the relaxation time ( $\tau$ ) dropped as the LiZnVO<sub>4</sub> percentage rose. Thus, the incorporation of conductive lithium ions into the dielectric PVDF produced an interfacial polarization, which resulted from the formation of interfacial areas between the PVDF and the nanofiller. Furthermore, as LiZnVO<sub>4</sub> concentration is increased, free volumes inside the host matrix are reduced, leading to an accumulation of Li<sup>+</sup> ions at the interfaces, which causes a drop in the value of  $\tau$ .

In the low-frequency range, the dominance of the Ohmic components over the capacitive nature of the nanocomposites causes the  $\tan \delta$  value to rise as a function of frequency.  $\tan \delta$  increased with increasing frequency and subsequently progressively dropped owing to the increase in capacitive constituents inside the synthesized films at 90 and 120 °C. This finding leads to shorter relaxation times at higher temperatures, where lithium ions have higher energy. The best value of  $\tan \delta$  has been attained for the nanocomposite containing 5 wt% of LiZnVO<sub>4</sub>, indicating that the nanofiller was well incorporated into the PVDF, and this confirms the XRD and FT-IR results. Because of its superior performance in amorphous areas, this material is highly suggested for use in lithium solid-state battery production.

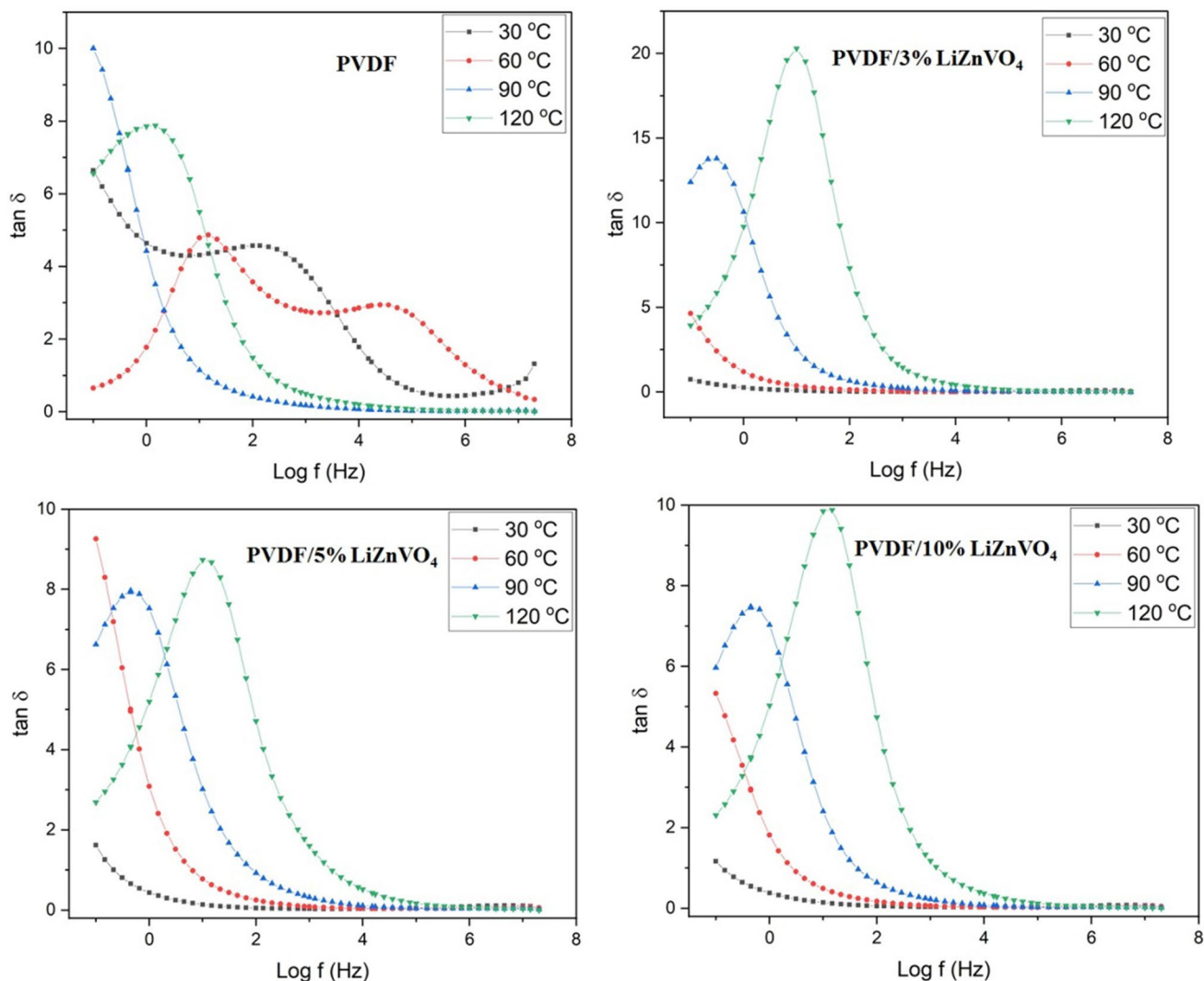


**Fig. 10** The variation of loss tangent ( $\tan \delta$ ) with frequency at 30 °C of PVDF and PVDF doped with a different weight percentage of LiZnVO<sub>4</sub> samples

### 3.4.3 Electric moduli analysis

The electric modulus formalism is mainly used to suppress the contribution of electrode polarization. By using standard formulae [48–51], we were able to calculate the real and imaginary moduli of dielectrics,  $M'$  and  $M''$ , respectively:

$$M' = \frac{\epsilon'}{\epsilon'^2 + \epsilon''^2} \text{ and } M'' = \frac{\epsilon''}{\epsilon'^2 + \epsilon''^2} \tag{7}$$

The dependence of  $M'$  on the frequency at 30 °C for the PVDF doped with various concentrations of LiZnVO<sub>4</sub> is exhibited in Fig. 11. The spectra in this figure are characterized by the existence of long-tail lies in the frequency range of (10—5 M) Hz. The presence of such a long tail indicates that the electrode polarization contribution has been eliminated. This finding also implies that the PVDF-based nanocomposite films have a remarkable capacitive feature.

This detected a reduction in  $M'$  values with increasing LiZnVO<sub>4</sub> contents up to the concentration of 5 weight % means that generated ions hop across locations, which indicates that hopping is the dominant conduction mechanism in the present films. It is shown in Fig. 12 how the  $M''$  values change with frequency for the nanocomposite samples when measured at 30 °C. The  $M''$  curves exhibit two distinct loss peaks caused by the movement of induced

**Fig. 11** The dependence of  $M'$  values on the frequency at 30 °C for PVDF and PVDF doped with a different weight percentage of  $\text{LiZnVO}_4$  samples

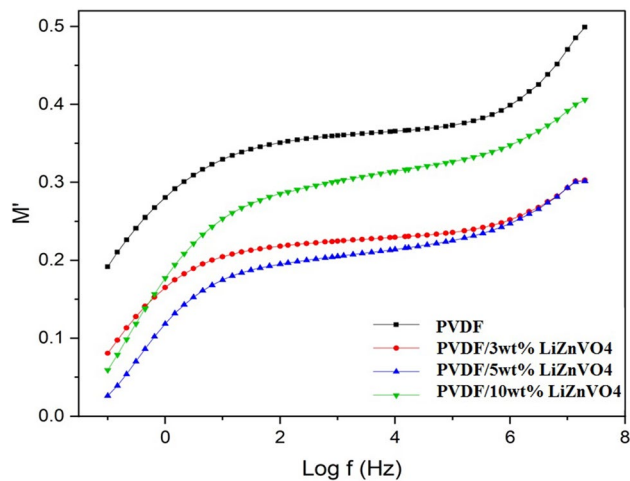


**Fig. 12** The change in  $M''$  values with frequency at 30 °C for PVDF and PVDF doped with a different weight percentage of  $\text{LiZnVO}_4$  samples

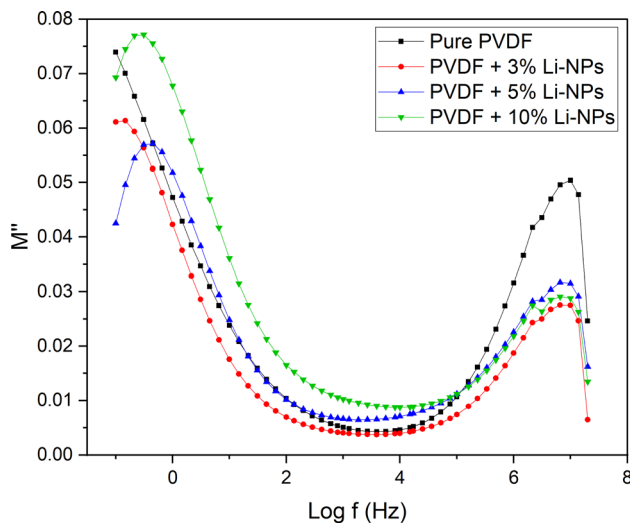
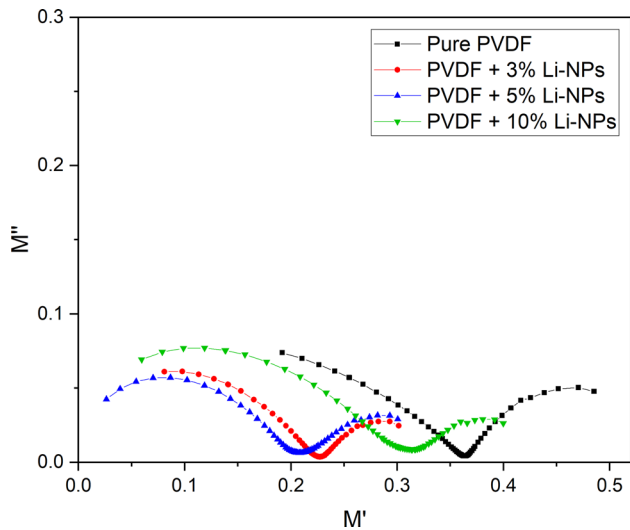


**Fig. 13** The variation of  $M''$  versus  $M'$  at 30 °C for PVDF and PVDF doped with a different weight percentage of  $\text{LiZnVO}_4$  samples



H<sup>+</sup> and Li<sup>+</sup> ions, implying that the host matrix central chain has been relaxed. The obvious change in the peak's intensities with the increase in the nanofiller percentage refers to the non-Debye behavior of the current nanocomposite films. The change is also largely in agreement with the dielectric relaxation stemming from Maxwell–Wagner–Sillars (MWS) polarization effect. The shift observed in the first characteristic relaxation peak toward higher frequencies is a solid indicator of the reduction in relaxation duration as the LiZnVO<sub>4</sub>% increases.

The variation of M'' versus M' for the PVDF/ x wt% LiZnVO<sub>4</sub> samples is exhibited in Fig. 13. The Cole–Cole plot is generally divided into three frequency-dependent regions; low, middle, and high-frequency regions. These three regions are ascribed to the grain boundary effect, the participation of grains, and the bulk conduction relaxation process, respectively. The present spectra are characterized by a single semicircular arc attributed to the grain boundary effect and surface polarization, while the observed peak is assigned to the bulk conduction response [44, 52]. The asymmetrical behavior of this relaxation peak verifies the non-Debye dielectric relaxation response. The relaxation peak frequencies are governed by the following equation:

$$f_{\max} \approx \frac{1}{2\pi RC} \quad (8)$$

According to this equation, the peak frequency is inversely proportional to the capacitance of the geometrical capacitor. Compared to the observed shift in the  $f_{\max}$  toward the lower frequency region, the PVDF/ 5wt% LiZnVO<sub>4</sub> nanocomposite sample has achieved the highest capacitance, recommending it to be used in designing Li-ion batteries. Further, this shift is a clear indication of the small contribution of the grain boundary to the electrical conduction mechanism inside the PVDF host matrix. This performance is attributed to the rotation of the dipoles, which supports the capacitive nature of the present nanocomposite film on resistive behavior and gives it valuable comparative advantages over other composites.

### 3.5 Electrical conduction mechanism

The frequency dependence of the above-described nanocomposite films' AC conductivity ( $\sigma_{ac}$ ) is shown in Fig. 14 at 30 °C. As the concentration of LiZnVO<sub>4</sub> increased, amorphous areas became more dominant, simplifying the transit of induced ions, and thus giving rise to the detected growth in  $\sigma_{ac}$ . Relaxation of ions via bouncing back and forth across localized sites increased with increasing frequency, resulting in the enhancement of electrical conductivity. The change in hopping behavior from long-range to short-range distances is responsible for this improvement.

The  $\sigma_{ac}$  curves may be broken down into three distinct parts: the low-frequency area (region I), which represents the DC conductivity ( $\sigma_{dc}$ ), whereas the second part (region II) reveals the dispersive region and is located at 100 Hz—5 MHz. The third segment (region III) is located at  $f < 5$  MHz, where the induced ions cannot follow the rapid rotation of the direction of the applied field, forming ion pairs and ion triplets, which affects their mobility and thus reduces the AC conductivity at this stage.

The jump relaxation model helps explain the three components of  $\sigma_{ac}$  curves. With this model, we can predict the likelihood of a successful return to your starting point based on the percentage of hops that succeed (i.e., returns to their original location). The observed variance in the  $\sigma_{ac}$  values for the PVDF-based nanocomposite samples is due to the fluctuation in

**Fig. 14** The dependency of AC conductivity ( $\sigma_{ac}$ ) onto the frequency at 30 °C for PVDF and PVDF doped with a different weight percentage of LiZnVO<sub>4</sub> samples

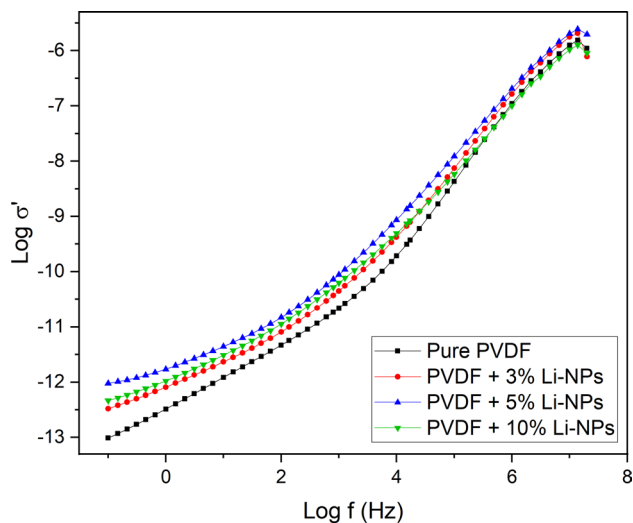


**Fig. 15** The change in  $\sigma_{ac}$  with frequency curves of the sample containing 5 weight percentage of  $\text{LiZnVO}_4$  (achieved the best performance) at various temperatures

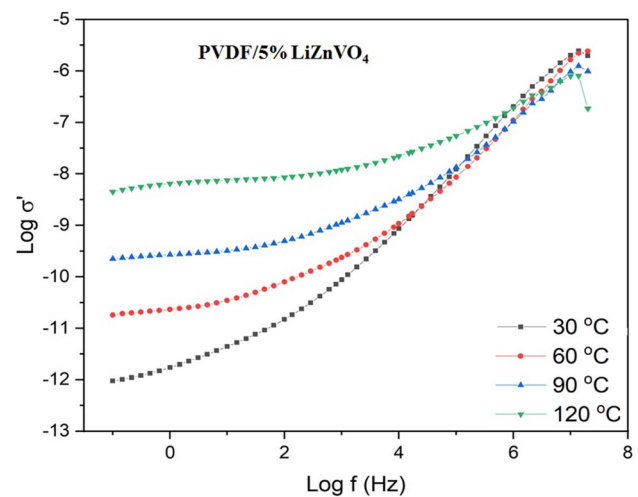
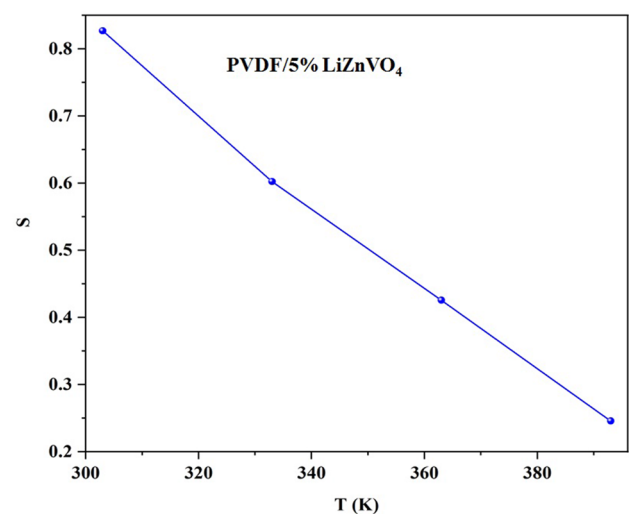


**Fig. 16** The investigated behavior of  $S$  values for the PVDF/5%  $\text{LiZnVO}_4$  nanocomposite



this ratio between successful and failed hops. Thus, the electrical conductivity of nanocomposite samples can be interpreted using Jonscher's universal power-law, and is represented as follows [43, 45, 46];

$$\sigma = \sigma_{dc} + A\omega^S \quad (9)$$

where  $A$  is a factor that depends on temperature.  $S$  is a frequency exponent, which affects by the translational movement of the induced ions during the electrical conduction process inside the PVDF/  $\text{LiZnVO}_4$  nanocomposite samples.

The variation of  $\sigma_{ac}$  with frequency curves of the sample containing 5 weight percentages of  $\text{LiZnVO}_4$  (achieved the best performance) at various temperatures is demonstrated in Fig. 15. The literature has reports of similar conduct. This figure illustrates how the  $\sigma_{ac}$  values rise with increasing sample temperature, highlighting how the induced ions inside the nanocomposite films become thermally active. The behavior of  $S$  values for the PVDF/5%  $\text{LiZnVO}_4$  sample investigated in the temperature range 30–120 °C is exhibited in Fig. 16, where a decrease in  $S$  values with the continuous increase in temperature is observed. This finding suggests that the associated barrier hopping model is best suitable for understanding and characterizing the ions' behavior throughout the conduction process within the present nanocomposites, confirming the above findings. These findings may be explained by the metastable migration of lithium ions from site Li (8a) to site V(16c) to site V(8a) at low temperatures. These results show that the  $\text{LiZnVO}_4$ -filled films analyzed have desirable properties, making them an excellent starting point for creating cutting-edge energy storage devices and lithium-ion batteries.

## 4 Conclusions

This research extracted the preparation and characterization of  $\text{LiZnVO}_4$  nanoparticles as a new nanomaterial. The prepared  $\text{LiZnVO}_4$  was combined with PVDF as a basic polymeric material whose properties need to be modified and improved for possible use in solid lithium battery applications. The structural, optical, and electrical properties of PVDF/ $\text{LiZnVO}_4$  nanocomposites were studied. The characteristic X-ray diffraction peaks of PVDF and  $\text{LiZnVO}_4$  were observed. The XRD spectra show the rhombohedral structure of  $\text{LiZnVO}_4$ . Scherrer's equation and W-L plot were used to determine the crystallite size and strain of  $\text{LiZnVO}_4$  and the result was determined to be 83 nm. The main characteristic IR bands of PVDF as a host material were detected. An interaction between PVDF and  $\text{LiZnVO}_4$  was approved by shifting some IR bands. The behavior of the energy band gap was decreased with increasing  $\text{LiZnVO}_4$  due to the formation of disorder and the density of the localized states in the mobility band gaps. The dielectric behavior of the PVDF/ $\text{LiZnVO}_4$  films has been investigated as a function of temperature and frequency. At the lower range of the frequencies, both  $\epsilon'$  and  $\epsilon''$  had their maximum values and began to decrease as the frequency and temperature increased. The Cole–Cole plots were divided into three frequency-dependent regions (low, middle, and high-frequency) which ascribed to the grain boundary effect, the participation of grains, and the bulk conduction relaxation process, respectively. The spectra were characterized by a semicircular arc attributed to the grain boundary effect and surface polarization, while the spike observed is assigned to the bulk conduction response. The prepared samples' electrical conductivity was described by the Jonscher universal power law, which suggests that they might provide an excellent foundation on which to build new and improved energy storage devices and lithium batteries.

**Acknowledgements** Not applicable.

**Author contributions** ISE: supervised the findings of this work, writing—original draft, review, and Editing. AMI: contributed to sample preparation, formal Analysis, investigation, writing-original draft AMA: conceived of the presented idea, carried out the experiments with A. M. Ismail, analysis, review, AYY: investigation, derived the models and analyzed the data of AC conductivity, writing an original draft, review. All authors discussed the results and contributed to the final manuscript.

**Funding** The authors declare that no funds, grants, or other support were received during the preparation of this manuscript.

**Data availability** The data that support the findings of this study are available from the corresponding author upon reasonable request.

## Declarations

**Ethics approval and consent to participate** Not applicable.

**Consent for publication** Not applicable.

**Competing interests** The authors declare that there is no conflict of interest regarding the publication of this paper.

**Open Access** This article is licensed under a Creative Commons Attribution 4.0 International License, which permits use, sharing, adaptation, distribution and reproduction in any medium or format, as long as you give appropriate credit to the original author(s) and the source, provide a link to the Creative Commons licence, and indicate if changes were made. The images or other third party material in this article are included in the article's Creative Commons licence, unless indicated otherwise in a credit line to the material. If material is not included in the article's Creative Commons licence and your intended use is not permitted by statutory regulation or exceeds the permitted use, you will need to obtain permission directly from the copyright holder. To view a copy of this licence, visit <http://creativecommons.org/licenses/by/4.0/>.

## References

1. Yoshino A. The birth of the lithium-ion battery. *Angew Chemie Int Ed.* 2012;51(24):5798–800. <https://doi.org/10.1002/anie.201105006>.
2. Choe HS, Giaccari J, Alamgir M, Abraham KM. Preparation and characterization of poly(vinyl sulfone)- and poly(vinylidene fluoride)-based electrolytes. *Electrochim Acta.* 1995;40(13–14):2289–93. [https://doi.org/10.1016/0013-4686\(95\)00180-M](https://doi.org/10.1016/0013-4686(95)00180-M).
3. Appetecchi GB, Croce F, Scrosati B. High-performance electrolyte membranes for plastic lithium batteries. *J Power Sources.* 1997;66(1–2):77–82. [https://doi.org/10.1016/S0378-7753\(96\)02484-6](https://doi.org/10.1016/S0378-7753(96)02484-6).
4. Song JY, Wang YY, Wan CC. Open Access Review of gel-type polymer electrolytes for lithium-ion batteries. *J Power Sources.* 1999;77:183–97. [https://doi.org/10.1016/S0378-7753\(98\)00193-1](https://doi.org/10.1016/S0378-7753(98)00193-1).
5. Stephan AM. Review on gel polymer electrolytes for lithium batteries. *Eur Polym J.* 2006;42(1):21–42. <https://doi.org/10.1016/j.eurpolymj.2005.09.017>.

6. Bai X, Li T, Dang Z, Qi YX, Lun N, Bai YJ. Ionic conductor of  $\text{Li}_2\text{SiO}_3$  as an effective dual-functional modifier to optimize the electrochemical performance of  $\text{Li}_4\text{Ti}_5\text{O}_{12}$  for high-performance Li-ion batteries. *ACS Appl Mater Interfaces*. 2017;9(2):1426–36. <https://doi.org/10.1021/acsami.6b10795>.
7. Lu J, Chen Z, Ma Z, Pan F, Curtiss LA, Amine K. The role of nanotechnology in the development of battery materials for electric vehicles. *Nat Nanotechnol*. 2016;11(12):1031–8. <https://doi.org/10.1038/nnano.2016.207>.
8. Elashmawi IS, Gaabour LH. Raman, morphology and electrical behavior of nanocomposites based on PEO/PVDF with multi-walled carbon nanotubes. *Results Phys*. 2015;5:105–10. <https://doi.org/10.1016/j.rinp.2015.04.005>.
9. Mohseni M, Ahmad AR, Shirazi FH, Nemati NH. Preparation and characterization of self-electrical stimuli conductive gellan based nano scaffold for nerve regeneration containing chopped short spun nanofibers of PVDF/MCM41 and polyaniline/graphene nanoparticles: Physical, mechanical and morphological. *Int J Biol Macromol*. 2021;167:881–93. <https://doi.org/10.1016/j.ijbiomac.2020.11.045>.
10. Gao Z, et al. Protection of Li metal anode by surface-coating of PVDF thin film to enhance the cycling performance of Li batteries. *Chinese Chem Lett*. 2019;30(2):525–8. <https://doi.org/10.1016/j.ccllet.2018.05.016>.
11. Elashmawi IS. Effect of NaCl filler on ferroelectric phase and polaron configurations of PVDF films. *Cryst Res Technol*. 2007;39(4):389–93. <https://doi.org/10.1002/crat.200610833>.
12. Su YP, Sim LN, Li X, Coster HGL, Chong TH. Anti-fouling piezoelectric PVDF membrane: Effect of morphology on dielectric and piezoelectric properties. *J Memb Sci*. 2021. <https://doi.org/10.1016/j.memsci.2020.118818>.
13. Zhao X, Li C, Qi R, Guo H, Peng G. Study on relaxation behavior of all-polymer PVDF-based films containing dielectric fluoroelastomer. *Polymer (Guildf)*. 2022;252(January):1–9. <https://doi.org/10.1016/j.polymer.2022.124933>.
14. Su YP, Sim LN, Coster HGL, Chong TH. Incorporation of barium titanate nanoparticles in piezoelectric PVDF membrane. *J Memb Sci*. 2021. <https://doi.org/10.1016/j.memsci.2021.119861>.
15. Santos BPS, et al. PVDF containing different oxide nanoparticles for application in oil and gas pipelines. *Mater Today Commun*. 2021. <https://doi.org/10.1016/j.mtcomm.2020.101743>.
16. Kim YK, Hwang SH, Seo HJ, Jeong SM, Lim SK. Effects of biomimetic cross-sectional morphology on the piezoelectric properties of  $\text{BaTiO}_3$  nanorods-contained PVDF fibers. *Nano Energy*. 2022. <https://doi.org/10.1016/j.nanoen.2022.107216>.
17. Ye Q, et al. Fabricating a PVDF skin for PEO-based SPE to stabilize the interface both at cathode and anode for Li-ion batteries. *J Energy Chem*. 2022;70:356–62. <https://doi.org/10.1016/j.jechem.2022.02.037>.
18. Widiyandari H, Ade Putra O, Purwanto A, Abidin Z. Synthesis of PVDF/ $\text{SiO}_2$  nanofiber membrane using electrospinning method as a Li-ion battery separator. *Mater Today Proc*. 2020;44:3245–8. <https://doi.org/10.1016/j.matpr.2020.11.448>.
19. Wang J, Deng Q, Li M, Jiang K, Hu Z, Chu J. High-capacity and long-life lithium storage boosted by pseudocapacitance in three-dimensional  $\text{MnO}-\text{Cu}-\text{CNT}/\text{graphene}$  anodes. *Nanoscale*. 2018;10(6):2944–54. <https://doi.org/10.1039/c7nr08191j>.
20. Grandhe BK, Ramaprabhu S, Buddhudu S, Sivaiah K, Bandi VR, Jang K. Spectral characterization of novel  $\text{LiZnVO}_4$  phosphor. *Opt Commun*. 2012;285(6):1194–8. <https://doi.org/10.1016/j.optcom.2011.10.013>.
21. Ram M. Structure and electrical conduction behavior of  $\text{LiZnVO}_4$  ceramic prepared by solution-based chemical route. *J Alloys Compd*. 2011;509(18):5688–91. <https://doi.org/10.1016/j.jallcom.2011.02.128>.
22. Kumar K, Suraj K, Dangi B, Dhayal V, Savas SK. Structural, optical, and surface morphological studies of ethyl cellulose/graphene oxide nanocomposites. *Polym Compos*. 2020. <https://doi.org/10.1002/pc.25576>.
23. Dhayal V, Hashmi SZ, Kumar U, Choudhary BL, Kuznetsov AE. Spectroscopic studies, molecular structure optimization and investigation of structural and electrical properties of novel and biodegradable Chitosan-GO polymer nanocomposites. *J Mater Sci*. 2020;55(30):14829–47. <https://doi.org/10.1007/s10853-020-05093-5>.
24. Shen H, et al. Simultaneously enhancing the performance and mobility of organic solar classical systems by a novel additive. *Opt Mater (Amst)*. 2023. <https://doi.org/10.1016/j.optmat.2022.113219>.
25. Liu X, Peng Y, Liang Z, Wang L, Han S, Dou Z. Efficient ternary organic photovoltaic device with a non-halogenated solvent via synergistic inhibiting charge. *J Mater Chem C*. 2023. <https://doi.org/10.1039/D2TC05161C>.
26. Tuichai W, Karaphun A, Ruttanapun C. Improved dielectric properties of PVDF polymer composites filled with Ag nanomaterial deposited reduced graphene oxide (rGO) hybrid particles. *Mater Res Bull*. 2022. <https://doi.org/10.1016/j.materresbull.2021.111552>.
27. Sato M, Ishii H, Sueda Y, Watanabe K, Nagao D. A reinforced, high- $\kappa$  ternary polymer nanocomposite dielectrics of PVDF, barium titanate nanoparticles, and TEMPO-oxidized cellulose nanofibers. *Compos Part C Open Access*. 2021. <https://doi.org/10.1016/j.jcom.2021.100163>.
28. Bicy K, Gueye AB, Rouxel D, Kalarikkal N, Thomas S. Lithium-ion battery separators based on electrospun PVDF: a review. *Surf Interfaces*. 2022. <https://doi.org/10.1016/j.surf.2022.101977>.
29. Wang Y, Huang K, Zhang P, Li H, Mi H. PVDF-HFP based polymer electrolytes with high  $\text{Li}^+$  transference number enhancing the cycling performance and rate capability of lithium metal batteries. *Appl Surf Sci*. 2022. <https://doi.org/10.1016/j.apsusc.2021.151593>.
30. Menazea AA, Ismail AM, Elashmawi IS. The role of  $\text{Li}_4\text{Ti}_5\text{O}_{12}$  nanoparticles on enhancement the performance of PVDF/PVK blend for lithium-ion batteries. *J Mater Res Technol*. 2020;9(3):5689–98. <https://doi.org/10.1016/j.jmrt.2020.03.093>.
31. Elashmawi IS. Effect of LiCl filler on the structure and morphology of PVDF films. *Mater Chem Phys*. 2008;107(1):96–100. <https://doi.org/10.1016/j.matchemphys.2007.06.045>.
32. Elashmawi IS, Abdelrazek EM, Ragab HM, Hakeem NA. Structural, optical and dielectric behavior of PVDF films filled with different concentrations of iodine. *Phys B Condens Matter*. 2010. <https://doi.org/10.1016/j.physb.2009.08.037>.
33. Elashmawi IS, Al-Muntaser AA, Ismail AM. Structural, optical, and dielectric modulus properties of PEO/PVA blend filled with metakaolin. *Opt Mater (Amst)*. 2022. <https://doi.org/10.1016/j.optmat.2022.112220>.
34. Elashmawi IS, Elsayed NH, Altalhi FA. The changes of spectroscopic, thermal and electrical properties of PVDF/PEO containing lithium nanoparticles. *J Alloys Compd*. 2014;617:877–83. <https://doi.org/10.1016/j.jallcom.2014.08.088>.
35. Abdelrazek EM, Elashmawi IS, Ragab HM. Manifestation of  $\text{MnCl}_2$  fillers incorporated into the polymer matrices in their dielectric properties. *Phys B Condens Matter*. 2008;403(18):3097–104. <https://doi.org/10.1016/j.physb.2008.03.012>.
36. Kumar S, et al. Journal of Electron Spectroscopy and Tailoring the structural, electronic structure and optical properties of Fe:  $\text{SnO}_2$  nanoparticles. *J Electron Spectrosc Relat Phenomena*. 2020. <https://doi.org/10.1016/j.elspec.2020.146934>.

37. Menazea AA, Alzahrani E, Shaltout AA. Gamma radiation introduces improvement in AC conductivity behavior and dielectric characterization of CuONPs@ PVP-PVA nano matrix films prepared by one—potential laser ablation method. *Opt Quant Electron*. 2022. <https://doi.org/10.1007/s11082-022-03635-6>.
38. Nough SA, Benthani K. Gamma induced changes in the structure and optical properties of ZnS/PVA nanocomposite. *J Vinyl Addit Technol*. 2019;25(3):271–7. <https://doi.org/10.1002/vnl.21689>.
39. Hussein KI, et al. Optical properties and novelty preparation PVA/PVP doping with Cu as surface plasmonic ions. *Optik (Stuttg)*. 2022. <https://doi.org/10.1016/j.ijleo.2022.168965>.
40. Elashmawi IS, AlMuntaser AA. Influence of—Co3O4 nanoparticles on the optical, and electrical properties of CMC/PAM polymer: combined FTIR/DFT study. *J Inorg Organomet Polym Mater*. 2021;31(6):2682–90. <https://doi.org/10.1007/s10904-021-01956-9>.
41. Yassin AY, Mohamed AR, Abdelghany AM, Abdelrazek EM. Enhancement of dielectric properties and AC electrical conductivity of nanocomposite using poly (vinyl chloride-co-vinyl acetate-co-2-hydroxypropyl acrylate) filled with graphene oxide. *J Mater Sci Mater Electron*. 2018;29(18):15931–45. <https://doi.org/10.1007/s10854-018-9679-7>.
42. Zhu J, et al. Carbon nanostructure-derived polyaniline metacomposites: Electrical, dielectric, and giant magnetoresistive properties. *Langmuir*. 2012;28(27):10246–55. <https://doi.org/10.1021/la302031f>.
43. Yassin AY. Dielectric spectroscopy characterization of relaxation in composite based on (PVA–PVP) blend for nickel–cadmium batteries. *J Mater Sci Mater Electron*. 2020;31(21):19447–63. <https://doi.org/10.1007/s10854-020-04478-1>.
44. Yassin AY. Impedance, structural and thermal analyses of polyvinyl alcohol/polyvinyl pyrrolidone blend incorporated with Li<sup>+</sup> ions for lithium-ion batteries. *J Mater Res Technol*. 2021;15:754–67. <https://doi.org/10.1016/j.jmrt.2021.08.063>.
45. Arya A, Sharma AL. Effect of salt concentration on dielectric properties of Li-ion conducting blend polymer electrolytes. *J Mater Sci Mater Electron*. 2018;29(20):17903–20. <https://doi.org/10.1007/s10854-018-9905-3>.
46. Wang Z, et al. Dielectric spectroscopy characterization of relaxation process in Ni/epoxy composites. *J Alloys Compd*. 2016;682:738–45. <https://doi.org/10.1016/j.jallcom.2016.05.025>.
47. Siva V, Vanitha D, Murugan A, Shameem A, Bahadur SA. Studies on structural and dielectric behaviour of PVA/PVP/SnO nanocomposites. *Compos Commun*. 2021. <https://doi.org/10.1016/j.coco.2020.100597>.
48. Bettaibi A, et al. Effect of erbium concentration on the structural, optical and electrical properties of a Bi<sub>4</sub>Ti<sub>3</sub>O<sub>12</sub> system. *RSC Adv*. 2017;7(36):22578–86. <https://doi.org/10.1039/c6ra27906f>.
49. Youssef AAA. The permittivity and AC conductivity of the layered perovskite [(CH<sub>3</sub>)(C<sub>6</sub>H<sub>5</sub>)<sub>3</sub>P]2HgI<sub>4</sub>. *Zeitschrift fur Naturforsch*. 2002;57(5):263–9. <https://doi.org/10.1515/zna-2002-0510>.
50. Ren S, et al. Dielectric relaxation behavior induced by lithium migration in Li<sub>4</sub>Ti<sub>5</sub>O<sub>12</sub> spinel. *J Alloys Compd*. 2019;793:678–85. <https://doi.org/10.1016/j.jallcom.2019.04.216>.
51. Yassin AY, Abdelghany AM. Synthesis and thermal stability, electrical conductivity and dielectric spectroscopic studies of poly (ethylene-co-vinyl alcohol)/graphene oxide nanocomposite. *Phys B Condens Matter*. 2021. <https://doi.org/10.1016/j.physb.2020.412730>.
52. Elashmawi IS, Ismail AM. Study of the spectroscopic, magnetic, and electrical behavior of PVDF/PEO blend incorporated with nickel ferrite (NiFe<sub>2</sub>O<sub>4</sub>) nanoparticles. *Polym Bull*. 2022. <https://doi.org/10.1007/s00289-022-04139-9>.

**Publisher's Note** Springer Nature remains neutral with regard to jurisdictional claims in published maps and institutional affiliations.